International Journal for Housing Science and Its Applications
Publish August 3, 2025. Volume 46, Issue 3 Pages 653-664

https://doi.org/10.70517/ijhsa46348

Distributed fiber optic sensing-based real-time monitoring technology for ±800kV high-voltage DC cable buffer layer faults

Gao Deng[1,*] and Zuopeng Zhang[1]
[1] Electronic Information School, Xi'an Polytechnic University, Xi'an, Shaanxi, 710600, China
Corresponding authors: (e-mail: 17829802698@163.com).

Abstract As the main transmission equipment of electric energy, cable is one of the key electric facilities to build stable and efficient power network. In recent years, ± 800kV high-voltage DC cable buffer layer erosion accidents, this paper launches the real-time monitoring research on the status of the cable. By analyzing the structure of the cable buffer layer and fault characteristics, the research foundation is laid. Then, the linear tensile test of the strain relationship between the high-voltage DC cable and the sensing fiber, as well as theoretical analysis, to establish the strain relationship between the high-voltage DC cable and the sensing fiber. Then the strain measured by the distributed fiber optic sensing technology is used to calculate the strain of the HVDC cable body and realize the monitoring of the HVDC cable. At the same time, the finite element method is used to establish the cable monitoring model and complete the strain calculation. In the K-fold cross validation, the average accuracy of the cable monitoring model based on distributed fiber optic sensing is 92.4% and relatively stable, with strong generalization ability as well as stability.

Index Terms buffer layer ablation, real-time monitoring, distributed fiber optic sensing, high-voltage DC cable

I. Introduction

China's rapid economic development and increasing productivity since the 20th century have resulted in an increasing demand for electric energy [1]. However, due to the vastness of China, the distribution of load centers and energy resources is not balanced, so large-scale long-distance transmission is required [2], [3]. In order to reduce the huge line loss caused by long-distance transmission, the voltage level of transmission lines has been gradually increased, and compared with AC transmission, DC transmission has the advantages of large long-distance transmission capacity and low line power loss [4]-[6]. Therefore, under the impetus of the growing demand for electricity and the continuous development of power electronics technology, DC transmission projects such as high-voltage DC transmission and flexible DC transmission are being constructed more and more [7]-[9]. In addition, both power cables and overhead lines are important carriers of DC transmission. Compared with overhead lines, although the structure of power cables is relatively complex and the cost required to manufacture the same length of cables is higher, the cables are simple to wire, have high reliability of power delivery, do not require the support of towers, and will not have a large impact on the environment when buried in the ground or laid on the seabed [10]-[13]. Therefore, at present, high-voltage DC power cables are increasingly used in flexible DC transmission systems [14].

After the commissioning of high-voltage DC cables, the aging deterioration of insulation will occur under the action of many factors, which include temperature, electric field, moisture, stress, etc., and the deterioration of insulation will cause the operational reliability of cables to decrease [15]-[17]. Secondly, the accumulation, transfer and disappearance of space charge in DC cables will also directly lead to the distortion of the electric field inside the dielectric, thus affecting the electrical properties of HVDC insulating materials in various aspects such as conductivity, breakdown and aging [18]-[20]. Therefore, the establishment of a real-time monitoring system for ±800kV high-voltage DC cable buffer layer faults is conducive to guaranteeing the good operating condition of the cable, which is a key link in maintaining the stability and safety of the rail transit power system [21], [22].

This paper starts from the perspective of the construction of the buffer layer of high-voltage DC cable, discusses in detail the main characteristics of the buffer layer failure and the electric field distribution characteristics of the cable, summarizes and analyzes the buffer layer ablation phenomenon as well as the causes. Combined with the fiber grating coupling mode theory and linear tensile theory, it explains the strain relationship between the high-voltage DC cable and the sensing fiber. And based on the finite element model method, use the sensing fiber

strain to calculate the high-voltage DC voltage strain, so as to construct the cable detection model based on distributed fiber optic sensing. Through the application experiment of cable temperature distribution detection and K-fold cross validation, the practical application results of the model are examined. The model is also used to carry out experiments of multi-physical quantity monitoring to expand the monitoring characteristics of cable faults.

II. High voltage cable buffer layer failure mechanism

II. A.Structural analysis of the buffer layer

The buffer layer is located between the inner sheath and the insulation shield, and its structure is shown in Fig. 1.The inner sheath of Chinese cables is mostly crumpled aluminum sheath, which has the functions of radial water-blocking, mechanical protection, and good electrical conductivity.

The buffer layer usually includes water-blocking tape, gold cloth and air gap. Water-resistant tape tightly wrapped around the surface of the insulation shield, gold cloth wrapped around the surface of the water-resistant tape, water-resistant tape and wrinkled aluminum sheath wave valley close contact with the aluminum sheath wave peaks between the air gap. Water-resistant tape usually consists of fluffy cotton, water-resistant powder and non-woven fabrics, used to buffer the interaction between the insulation shield layer and the inner sheath, reducing the internal thermal expansion of the cable caused by the insulation shield layer - the inner sheath between the compressive stress. The water-blocking powder in the water-blocking tape absorbs water and expands to block water in the radial direction. The main component of water-resistant powder is sodium polyacrylate, which is weakly alkaline, and also contains monomer CM (chlorinated polyethylene), crosslinking agent, initiator and deionized water.

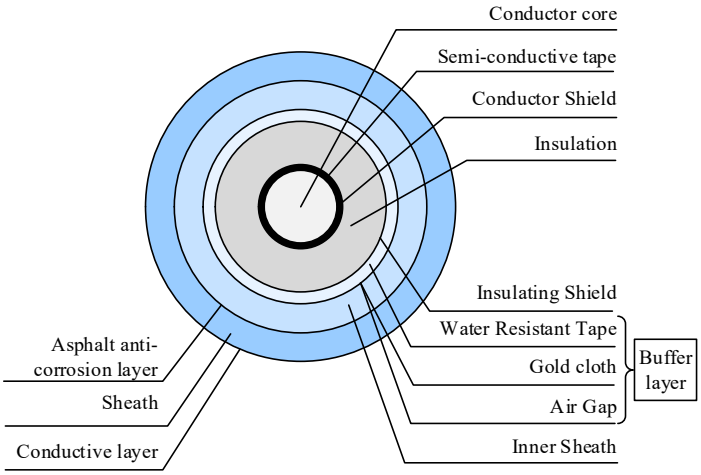

Figure 1: Cable profile

II. B.Buffer layer fault characterization

In the current high-voltage XLPE cables, the wrinkled aluminum sheath is the most widely used metal sheath structure in practice, and its axial structure is shown in Figure 2.

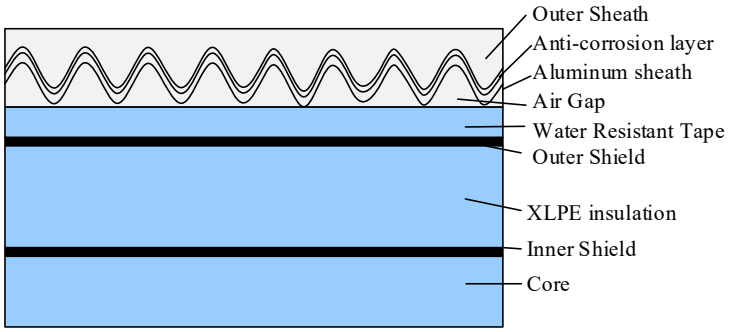

Figure 2: High voltage XLPE cable axial structure

Through the observation and analysis of the buffer layer ablation typical failure cases, found that the following characteristics: cable body on the existence of multiple ablation points, these ablation points are distributed in the metal aluminum jacket, semi-conductive buffer layer and the main insulation outside the semi-conductive layer. Ablation site has a large number of white water-blocking powder precipitation, semi-annular distribution, and the phenomenon has nothing to do with the location of the cable. Ablation is mainly concentrated in the wrinkled aluminum sheath inside the raised parts (i.e., the location of the trough). The degree of ablation and wrinkled aluminum sheath contact degree has a certain degree of correlation, wrinkled aluminum sheath and semiconducting buffer tape contact the more closely, the more serious the ablation, and the metal sheath is not tightly adhered to the circumference of the surface is rarely obvious ablation point.

Based on the above characteristics of the buffer layer erosion failure, the cause of the failure may be the buffer layer can not keep the insulation shielding layer and the metal sheath of good electrical contact between the buffer layer, resulting in the buffer layer inside the suspended potential, and this suspended potential will make the buffer layer inside the air gap field strength increases, once more than the air breakdown field strength, it will trigger a partial discharge. Localized discharge continues to develop, will eventually cause cable insulation breakdown.

II. C.Characterization of electric field distribution

Single-core conductor structure of high-voltage XLPE cable, the theoretical calculation of the electric field distribution is usually used concentric cylinder structure see Figure 3.

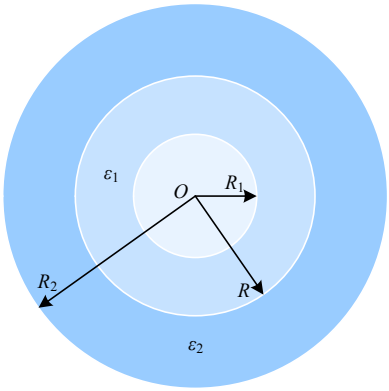

Figure 3: Cable concentric cylinder structure

Assuming that the radius of the shield of the cable core is R_1 and the radius of the outer surface of the insulation is R_2, when the cable is subjected to AC or impulse voltage U, the electric field strength at any point r from the center of the core is given in equation (1):

$$E = (U / r)\ln(R_2 / R_1) \tag{1}$$

For high-voltage XLPE cables, the dielectric properties of the cross-linked polyethylene main insulation and the semi-conductive shielding layer, water-blocking tape are very different, belonging to different properties of the medium. In order to calculate the electric field distribution in the multilayer structure of XLPE cables, select any two layers, such as Figure 3 shows the medium 1 and medium 2, the relative dielectric constant of ε_1 and ε_2, R_1 for the inner diameter of the medium 1, R_2 for the outer diameter of the medium 2, R for the intersection line of the medium 1 and medium 2.

The electric field distribution in dielectric 1 and dielectric 2 can be found according to Gauss's law:

When $R_1 < r < R$, there is equation (2):

$$E_1 = \frac{2\pi\Delta u}{\ln\frac{R}{R_1}\left(\frac{1}{\varepsilon_1}+\frac{1}{\varepsilon_2}\right)} = \frac{\Delta u}{r\varepsilon_1\left(\frac{\ln\frac{R}{R_1}}{\varepsilon_1}+\frac{\ln\frac{R_2}{R}}{\varepsilon_2}\right)} \tag{2}$$

When $R < r < R_2$, there is equation (3):

$$E_2 = \frac{2\pi\Delta u}{\ln\frac{R_2}{R}\left(\frac{1}{\varepsilon_1}+\frac{1}{\varepsilon_2}\right)} = \frac{\Delta u}{r\varepsilon_2\left(\frac{\ln\frac{R}{R_1}}{\varepsilon_1}+\frac{\ln\frac{R_2}{R}}{\varepsilon_2}\right)} \tag{3}$$

Semi-conductive cushioning, water-blocking tape structural characteristics are shown in Figure 4, it is usually composed of a layer of semi-conductive nonwoven fabric and a layer of semi-conductive fluffy cotton of about 1.5mm thickness, coated with a layer of polyacrylate expansion powder in the middle.

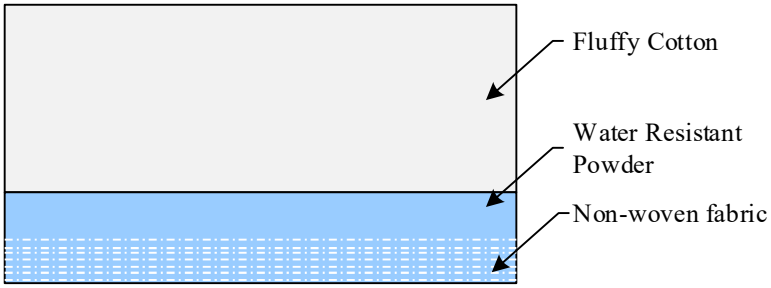

Figure 4: The structure of semiconductor buffer and water block

Although the semi-conductive fluffy cotton has semi-conductive properties, but the loose and porous structure makes it less conductive. The polyacrylate expansion powder itself does not have the conductivity to meet the water-blocking requirements. These factors lead to the cable insulation core and metal sheath (shielding) contact ability to decline, semi-conductive insulation shielding in suspension potential state. With the rise of the voltage on the cable, this suspended potential is also higher, and then there is a poor contact class discharge, and the amount of discharge with the rise in voltage and rise.

III. Cable monitoring model based on distributed fiber optic sensing

Fiber grating is an optical fiber-based sensor with unique advantages such as high sensitivity, high accuracy, and distribution monitoring capability. Therefore, this chapter explores the relationship between the fiber grating system and the strain of high-voltage DC cables based on the sensing mechanism of the fiber grating system. The finite element method is borrowed to establish a cable monitoring model based on distributed optical fiber.

III. A. Fiber grating coupling mode theory

Fiber Bragg gratings are made by photochemically treating an optical fiber using a UV laser or UV laser beam. The UV laser causes the refractive index in the fiber to change periodically along the core direction, enabling periodic refractive index modulation, which can also be described as a grating. When the wavelength of the incident light wave is equal to the Bragg wavelength (i.e., when the wavelength of the incident light wave is divided by two times the effective refractive index in the fiber is equal to the period of the grating), the Bragg condition will be satisfied and the incident light wave will be reflected by the Bragg grating. The rest of the wavelength will not be affected by the grating and will continue to be transmitted. The coupled mode theory is to analyze the transmission characteristics of light waves in the fiber core, using the solution of the optical waveguide to discuss the Bragg wavelengths as well as other wavelengths that are almost unaffected.

According to the set of electromagnetic field propagation equations, the fluctuation equations of light waves in fiber Bragg gratings are introduced as Eqs. (4)-(5):

$$\nabla^2 E + k_0^2 n^2 E + \nabla\left(E\cdot\frac{\nabla\varepsilon}{\varepsilon}\right) = 0 \tag{4}$$

$$\nabla^2 H + k_0^2 n^2 H + \frac{\nabla\varepsilon}{\varepsilon}\times(\nabla\times H) = 0 \tag{5}$$

In the above equation $k_0 = \omega\sqrt{\mu_0\varepsilon_0}$ is the reciprocal of the wavelength in vacuum. $n^2 = \varepsilon/\varepsilon_0$, and since the ε of the Bragg fiber is a constant value and $\nabla\varepsilon = 0$, the simplification of the fluctuation equations of the light wave leads to Eqs. (6)-(7):

$$\nabla^2 E + k_0^2 n^2 E = 0 \tag{6}$$

$$\nabla^2 H + k_0^2 n^2 H = 0 \tag{7}$$

All arbitrary light rays are expressed in fiber propagation as Eqs. (8)-(9):

$$E(x,y,z,t) = e(x,y)e_{\omega}^{i(\beta z-\omega t)} \tag{8}$$

$$H(x,y,z,t) = h(x,y)e_{\omega}^{i(\beta z-\omega t)} \tag{9}$$

β is the propagation constant, $e(x,y)$ is the electric field mode field, and $h(x,y)$ is the mode field of the magnetic field. Introducing them into the fluctuation equation leads to the eigen solutions as in Eqs. (10)-(11):

$$E_v(x,y,z,t) = e_v(x,y)e^{i(\beta_v z-\omega t)} \tag{10}$$

$$H_v(x,y,z,t) = h_v(x,y)e^{i(\beta_v z-\omega t)} \tag{11}$$

Assuming that the optical field propagates in the fiber, the waveguide is free of defects, the refractive index distribution is uniform and regular, and the coupled field propagates in the z-axis of the fiber is expressed as Eqs. (12)-(13):

$$E = (x,y,z,t) = \sum\left(A_v e^{i\beta_v z} + B_v e^{-i\beta_v z}\right)e_v(x,y)e^{-i\beta_v z} \tag{12}$$

$$H(x,y,z,t) = \sum\left(A_v e^{i\beta_v z} + B_v e^{-i\beta_v z}\right)h_v(x,y)e^{-i\beta_v z} \tag{13}$$

where A_v and B_v represent the magnitude of the retarded variables propagating positively and negatively along the Z axis of the fiber, respectively. The superposition of each eigenmode can be expressed in terms of the electromagnetic field, from which the coupled mode equations can be derived as Eqs. (14)-(15):

$$\begin{aligned}\frac{dA_v}{dz} &= iA_v\left(K_{vu}^t + K_{vu}^z\right)e^{i(\beta_v+\beta_v)z} \\ &+i\sum B_v(K_{vu}^t - K_{vu}^z)e^{-i(\beta_v+\beta_v)z}\end{aligned} \tag{14}$$

$$\begin{aligned}\frac{dB_v}{dz} &= iA_v\left(K_{vu}^t + K_{vu}^z\right)e^{i(\beta_v+\beta_v)z} \\ &-i\sum B_v\left(K_{vu}^t - K_{vu}^z\right)e^{-i(\beta_v+\beta_v)z}\end{aligned} \tag{15}$$

where K_{vu}^z is the longitudinal coupling coefficient between the u-order and v-order modes, K_{vu}^z □ K_{vw}^t for Bragg fiber modes, and is therefore negligible. There are Eqs. (16)-(17) when only the coupling of the forward transfer reverse transfer mode is considered:

$$\frac{dA}{dz} = iAk_{11} + iBke^{-i2\delta z} \tag{16}$$

$$\frac{dB}{dz} = -iBk_{11} - iAk^* e^{i2\delta z} \tag{17}$$

where $k_{11} = \frac{2\pi}{\lambda}\delta n_{\text{eff}}$, $k = \frac{k_{12}}{2} = \frac{k_{21}^*}{2} = \frac{\pi}{\lambda}\delta n_{eff}$, n_{eff} are the effective refractive indices of the fiber core, and δ is the phase mismatch quantity, which is mathematically expressed as equation (18):

$$\delta = \beta - \frac{\pi}{\Lambda} \tag{18}$$

where β is the propagation constant at any wavelength and Λ is the grid period. Disregarding the self-coupling term leads to Eqs. (19)-(20):

$$\frac{dA}{dz} = iBke^{-i2\delta z} \tag{19}$$

$$\frac{dB}{dz} = -iAk^* e^{i2\delta z} \tag{20}$$

Selecting an FBG grating of length L, Eq. (21) is obtained in accordance with the boundary conditions of the fiber grating waveguide:

$$A(0) = 1, B(L) = 0 \tag{21}$$

When $k^2 < \delta^2$, the reflectivity of the fiber Bragg grating is expressed as equation (22):

$$R = \frac{|B(0)|^2}{|A(0)|^2} = \frac{kk^* \sinh^2(sL)}{s^2\cosh^2(sL) + \delta^2\sinh^2(sL)} \tag{22}$$

The transmittance of the fiber Bragg grating is expressed as equation (23):

$$T=\frac{\left|A(L)\right|^2}{\left|A(0)\right|^2}=\frac{s^2}{s^2\cosh^2(sL)+\delta^2\sinh^2(sL)} \tag{23}$$

Thus it follows that $R+T=1$, and when δ is zero, there are equations (24)-(25):

$$R_{\max}=\tanh^2(kL) \tag{24}$$

$$T_{\max}=\cosh^2(kL) \tag{25}$$

It can be seen that the transmission of light waves in the fiber core and the exchange of power between various styles can be accurately described by the theory of fiber grating coupling modes.

III. B. Theoretical analysis of linear tensile test

The high-voltage DC cable is cylindrical, and the structural components of each layer are symmetrically distributed around the center of the axis. In order to establish a theoretical model of the strain relationship between the high-voltage DC cable and the sensing optical fiber, this section calculates from the perspective of geometric analysis.

For the convenience of analysis, it is assumed that the volume of the high-voltage DC cable remains unchanged during the stretching process, there is no relative displacement between the layers of the structural components of the high-voltage DC cable, and the change in the diameter of the optical unit is ignored. Optical unit stranded structure and high-voltage DC cable before and after stretching along the axial expansion, L is the stranded pitch of the optical unit of the high-voltage DC cable, r is the distance between the axis of the optical unit and the axis of the conductor, Lg is the length of the optical unit in a pitch, θ is the angle of stranding of the optical unit, Δr is the radial change of the high-voltage DC cable after stretching, ΔL is the length change of the high-voltage DC cable. Is the length change of the HVDC cable, and ΔLg is the length change of the optical unit.

According to before and after stretching, the volume of the HVDC cable is unchanged can be obtained from equation (26):

$$\pi r^2 L=\pi(r+\Delta r)^2(L+\Delta L) \tag{26}$$

Eqs. (27)-(28) can be obtained from the collinearity theorem:

$$L^2+(2\pi r)^2=Lg^2 \tag{27}$$

$$(L+\Delta L)^2+\left[2\pi(r+\Delta r)\right]^2=(Lg+\Delta Lg)^2 \tag{28}$$

Associative equations (26) and (28) lead to equation (29):

$$(L+\Delta L)^2+4\pi^2\frac{r^2L}{L+\Delta L}=(Lg+\Delta Lg)^2 \tag{29}$$

Associative equations (27) and (28) lead to equation (30):

$$(L+\Delta L)^2+\frac{(Lg^2-L^2)L}{L+\Delta L}=(Lg+\Delta Lg)^2 \tag{30}$$

Let $L+\Delta L=L(1+\varepsilon_L)$, and $Lg+\Delta Lg=Lg(1+\varepsilon_{Lg})$ leads to equation (31):

$$\varepsilon_{Lg}=\sqrt{\frac{\sin^2\theta\left((1+\varepsilon_L)^3-1\right)+1}{1+\varepsilon_L}}-1 \tag{31}$$

where ε_L and ε_{Lg} are the strains of the HVDC cable and the optical unit. Since the strain value is generally very small before the HVDC cable breaks, the product, square and cubic terms of the strain in Eq. (31) can be neglected, and then a simplified formula can be obtained as Eq. (32):

$$\varepsilon_{Lg}=\frac{3\sin^2\theta-1}{2}\varepsilon_L \tag{32}$$

In the strain of the high-voltage DC cable and the optical unit, with the increase of the strain of the high-voltage DC cable, since the strain of the optical unit calculated by the simplified formula is slightly smaller than that calculated by the original formula before the simplification, but it is basically the same within 6%, and the high-voltage DC cable is already broken when it is stretched to this strain, the strain relationship between the high-voltage DC cable and the optical unit can be described by the simplified formula.

In addition, the optical fiber generally exists in the optical unit with a residual length of about 0.5%, and the optical unit will first consume the fiber residual length at the beginning of the stretching stage, and will transfer the strain to the optical fiber after the residual length is consumed, so the effect of the fiber residual length needs to be

added to the calculation of the strain of the high-voltage DC cable based on the fiber strain measured by the distributed fiber-optic sensing device in Eq. (32). At the same time, it can be seen from Eq. (32) that in a certain strain range, the optical unit and the high-voltage DC cable should become an approximate linear relationship. The coefficient of the strain relationship between the two is related to the stranding angle of the optical unit, the larger the angle the larger the coefficient, the larger the strain of the optical unit under the same strain of the high-voltage DC cable.

III. C. Finite element modeling

YJQ42 high-voltage DC cable has a complex structure with 12 layers, and the high-voltage DC cable model is simplified in order to reduce the amount of calculation. Conductor shielding and insulation shielding and XLPE insulation mechanical parameters are approximate, can be merged into the insulation layer. Semiconductor water-blocking tape and brass tape thickness is small, poor mechanical properties, merged into the structure with similar properties in its neighborhood. In straight line stretching, the steel wire pinned mounting layer has no effect on the optical unit stranding layer, so the layers outside the optical unit layer do not need to be built up. Finally, the HVDC cable is simplified into six parts: copper conductor, XLPE insulation, lead alloy sheath, HDPE sheath, optical unit and PET filler strip, and the related parameters are shown in Table 1.The overall strain of the HVDC cable and the strain of the HDPE sheath are equal, so the HDPE sheath strain can be extracted as the overall strain of the HVDC cable.

Table 1: Collection dimensions and parameters of submarine cable components

Name	Density (t/cm3)	Elasticity modulus (0.1Mpa)	Poisson ratio	Geometrical parameter(cm)	
				Thickness	Calculated outside diameter
Copper conductor	$8.51*10^{-6}$	$1.3*10^{6}$	0.341	-	2.09
XLPE insulation	$1.40*10^{-6}$	$1.41*10^{4}$	0.302	2.176	6.42
Aluminium alloy sheath	$9.01*10^{-6}$	$2.02*10^{5}$	0.400	0.401	7.22
HDPE sheath	$1.12*10^{-6}$	$9.01*10^{3}$	0.301	0.496	8.23
Optical unit	$2.62*10^{-6}$	$7.02*10^{5}$	0.272	0.6	9.78
PET filler strip	$1.73*10^{-6}$	$6.51*10^{5}$	0.300	0.6	9.78

The high-voltage DC cable is 10 meters long, and the unit type of each component is a three-dimensional explicit structure SOLID164 solid unit composed of 8 nodes, and the material type is selected isotropic elastic material. Sweep mesh delineation method is used for uniform meshing of the components. The cross-section of the optical unit is relatively small, in order to increase the degree of realism of the model, the optical unit is encrypted, and finally the high-voltage DC cable finite element model is established.

The structure of the HVDC cable is complex, and mutual contact occurs between the layers of the HVDC cable, between the optical unit and the PET filler strip, and between the PET filler strips, and the direction of contact is difficult to accurately determine. Automatic contact settings can be used, which are automatically recognized by the computer according to the actual contact situation to improve the modeling speed. At the same time, the cross section of one end of the HVDC cable is fixed, i.e., constraints in all directions are applied to the nodes in that cross section. At the other end, an axial displacement load is applied, ranging from 0 to 8%, with a loading time of 8 s and a time step of $9*10^{-5}$ s. Finally, the model is solved.

IV. Testing and evaluation of model performance

In this chapter, we address the needs of distributed temperature monitoring and multi-physical quantity feature monitoring for HVDC cables, and firstly, we examine the performance of a cable monitoring model based on distributed fiber-optic sensing in terms of temperature distribution. Then, electromagnetic-thermal coupling simulation experiments and temperature monitoring are carried out successively to explore the possibility of applying temperature characteristic signals to the monitoring model. Finally, the accuracy of the model for fault monitoring is verified by K-fold cross validation to assess the effectiveness of the model in this paper.

IV. A. Monitoring and analysis of cable temperature distribution

Applying the model of this paper to the D cable monitoring system, Fig. 5 shows the results of distributed measurements taken by the D system on June 23, 2022 on the cable to be tested. From the figure, it can be seen that the load current is around 80 A until 06:00 a.m., and thereafter continues to rise to around 170 A. It reaches the morning peak of 162.12 A at 12:00 a.m., decreases and continues to maintain around 135 A, and reaches the peak electricity consumption of 170.25 A near 20:00 a.m. According to the principle of thermal circuit, it can be seen that

due to the presence of the heat capacity of an object resulting in the process of heat generation and dissipation are not Not synchronized, high-voltage cable in the temperature of each structure should lag behind the change in load current, but depends on the specific heat capacity of the object itself and the size of the mass. The process of heat generation in the conductor and heat dissipation through the skin takes time. The load current reaches its morning peak of 162.12 A at 12:00, and the ambient temperature peaks at 23.9°C near 14:00, both of which together result in a maximum measured temperature of 24.39°C near 14:00. On the day of the experiment, the overall load current amplitude of the cable under test was at a low level and the current change was not obvious, and the internal heat generation of the conductor was less, so the measurement results depended more on the influence of the temperature change in the environment on the cable temperature, and therefore it was considered that the hysteresis of the temperature change due to the heat capacity of the material had an acceptable influence on the experimental results.

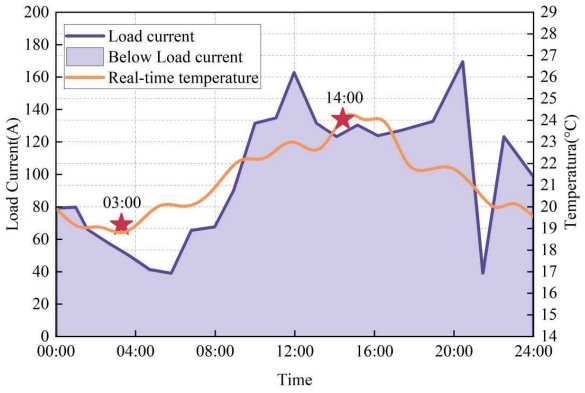

Figure 5: The experimental results of the cable temperature monitoring

In Fig. 5 it can be seen that between 00:00 and 04:00 the ambient temperature hardly changes while the measured temperature decreases as the load current decreases. Around 12:00, the ambient temperature is decreasing, while the measured temperature increases as the load current increases. There is a positive correlation between the measured temperature and the load current. Between 12:00 and 19:00 the load current changes very little, and the trend of the measured temperature is also correlated with the ambient temperature. The experimental results show that the minimum temperature of the cable to be measured at 03:00 a.m. is 18.888°C, and the maximum temperature of the cable to be measured at 14:00 p.m. is 24.298°C. The measured external surface temperature of the cable to be measured at 14:00 p.m. is 24.298°C. The measured outer skin temperature of the cable to be tested rises gradually with the increase of ambient temperature, and when the load current rises and the external ambient temperature is approximately constant, the measured outer skin temperature of the cable to be tested rises with the increase of load current.

Fig. 6 shows the change curve of conductor temperature calculated according to the fitting formula with the simulated conductor temperature and the error relationship between the two.

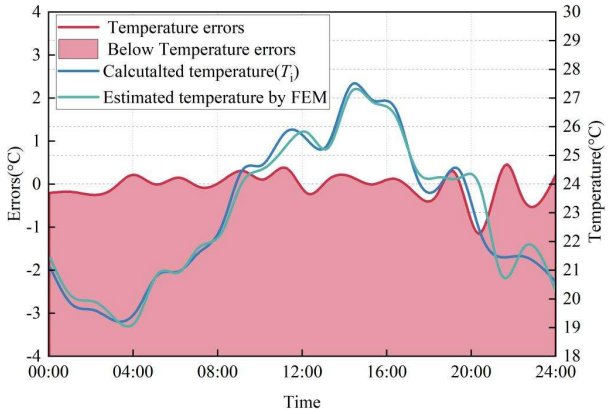

Figure 6: A comparison of the cable conductor temperature calculation results

As can be seen from Fig. 6, the calculated cable conductor temperature is basically consistent with the temperature results obtained from the electromagnetic-thermal coupling simulation, with a maximum error of about 2.5°C. Due to the low temperature on the day of the measurement, the actual load currents are at a low level, with a maximum load current of no more than 200 A, and the heat losses generated by the conductor energization are also very small. In this case, the heat exchange process is very slight. The influence of the ambient temperature and the variation of the load current together determine the measurement results, resulting in an error of only about 2.5°C. The measurement results are based on the ambient temperature and the load current. When the cable is in an unstable environment and the load current continues to rise significantly, the heat loss in the cable increases and the heat exchange process intensifies, at which point the error may change. In addition, the temperature error increases with sudden changes in load current, which is due to the time delay in the temperature change between the cable's outer skin and the inner conductor.

In summary, with the algorithmic support of the model proposed in this paper, the monitoring system can realize the distributed temperature monitoring of the outer skin of the cable, and calculate the temperature of the cable conductor under different ambient temperatures and load currents by monitoring the obtained outer temperature.

IV. B. Multi-physical monitoring

IV. B. 1) Simulation experiments based on finite elements

In this subsection, the finite element method is used to investigate the temperature distribution characteristics of the cable buffer layer region under electro-thermal coupling by applying the model proposed in this paper. The effects of the conductivity of the buffer layer material, σ_b, and the length of the poor electrical contact, L_{insul}, on the maximum temperatures inside and outside the ablation region of the buffer layer, θ_1, θ_2, and the intensity of the internal heat source, Q. The results of the effects of different conductivities and electrical contacts on the ablation region are shown in Fig. 7. As can be seen from the figure, θ_1 andθ_2 have a similar trend of change, which are both monotonically rising with the decrease in the conductivity and monotonically increasing with the prolongation of the length of poor electrical contact. Figures 7(b) and 7(d) give the variation of the intensity of the heat source. When the conductivity decreases, the resistance of the buffer layer rises, the Joule heat generated increases and the temperature rises. When the length of the longitudinal electrical contact failure increases, the current concentration increases, again leading to a rise in temperature. Under extreme conditions, the internal heat source intensity at the ablation site can be as high as 9.7x10^{7}W/m^3. Conductivity is an intrinsic property of the buffer layer material, and both it and the degree of electrical contact malpractice have a significant effect on the heating phenomenon at the ablation site.

Experiments have shown that when the conductivity of the buffer layer deteriorates, or the cable longitudinal electrical contact is poor, the local area will be high temperature, the buffer layer ablation area of the highest temperature exceeds the thermal decomposition temperature of the buffer layer material, which in turn releases small molecule gases, produces local hot spots, resulting in ablation failure.

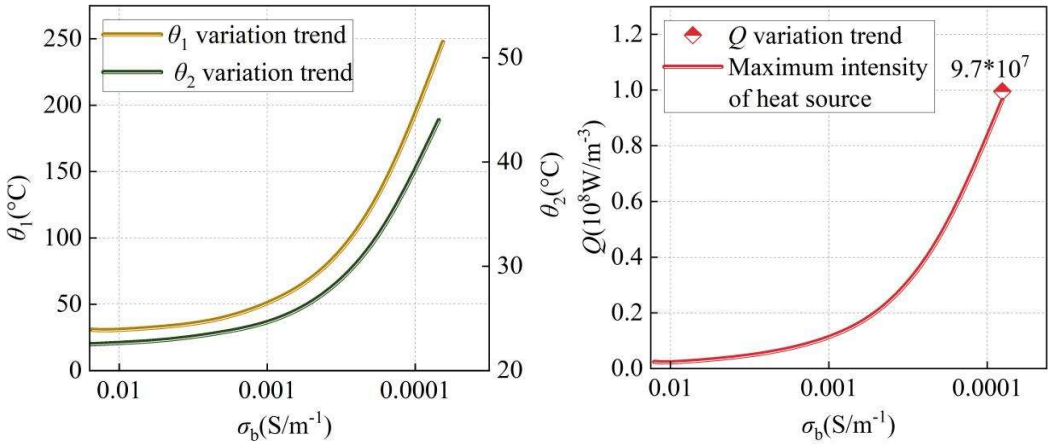

(a) The curve of θ1, θ2 versus σb

(b) The curve of Q versus σb

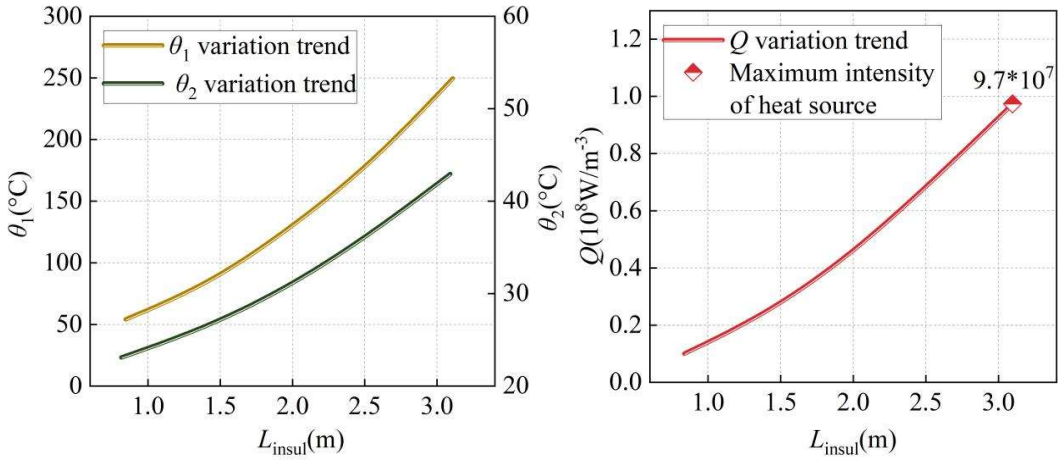

(c) The curve of θ1, θ2 versus Linsul (d) The curve of Q versus Linsul

Figure 7: Influence of poor conductivity and electrical contact on ablative region

IV. B. 2) Temperature monitoring results

This subsection is based on the proposed model to carry out the study of the temperature and evolution law generated by the buffer layer ablation process.

In the unpressurized state, change the water content (mass fraction) of the buffer layer sample and carry out the ablation experiment, record the change rule of the buffer layer center temperature with the ablation time is shown in Fig. 8. It can be found that the temperature of the buffer layer in the unpressurized state rises slowly at the beginning of the application of the current, and then there are several times of the temperature rises suddenly as well as decreases, i.e., the existence of a number of sudden changes in the temperature peaks. In addition, the presence of moisture will make the appearance of the temperature peaks earlier, the higher the water content, the more significant temperature anomalies.

In the dry state, the mass of the weight above the buffer layer sample was changed to regulate the contact pressure between the electrode and the buffer layer, and the change rule of the temperature of the buffer layer center with the ablation time was recorded in Fig. 9, which shows that the temperature of the buffer layer in the pressurized state always rises slowly, and the buffer layer warms up more slowly under higher pressure. The whole ablation process did not appear temperature peaks, which is significantly different from the characteristics of the temperature change in the ablation of the non-pressurized state.

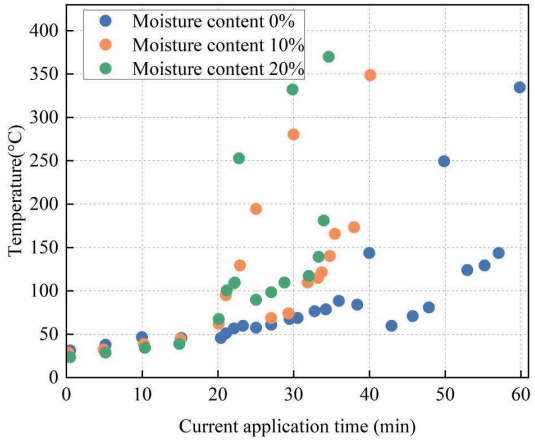

Figure 8: The variation trend of different temperature with current time

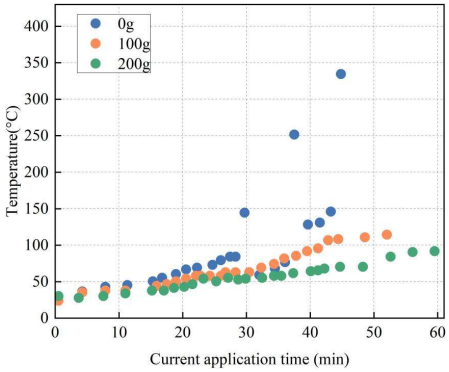

Figure 9: Temperature variation trend of dry buffer layer under pressure

Experiments show that temperature can be used as a characteristic signal of buffer layer ablation, which is more sensitive to the ablation process of the buffer layer in different water quantity states.

IV. C. K-fold cross validation

To further evaluate the generalization and stability of the model proposed in this paper, K-fold cross validation is performed on simulated data.K-fold cross validation divides the simulated dataset into K equal number of subsets, using (K-1) of these subsets for training, and then testing on one of the remaining subsets. This is repeated K times, with each subset being used as a test set once, and the results are eventually averaged to more reliably estimate the performance of the model. Table 2 demonstrates the results of K-fold cross validation, in this study K=5. As can be seen from Table 2, the average accuracy of K-fold cross validation is 92.4% and the accuracy of each K-fold cross validation is relatively stable, which indicates that the algorithm in this paper has a good generalization ability and stability.

Table 2: K-fold cross-validation results on the test dataset

Number of folds	1	2	3	4	5	Average
Accuracy rate (%)	93	90	94	92	93	92.4

V. Conclusion

For the high-voltage DC cable buffer layer can not be continuously insulated good electrical contact, resulting in buffer layer ablation accident. In this paper, the distributed fiber optic strain is used to calculate the strain of high-voltage DC cables, and a real-time monitoring method of the cable status is proposed.

(1) Based on the fault characteristics of high-voltage DC cable buffer layer, distributed fiber optic sensing technology is used as the core technology for real-time fault monitoring. Establish the strain relationship equation between the high-voltage DC cable and the distributed optical fiber during linear stretching, and use the strain measured by the distributed optical fiber sensing technology to calculate the cable body strain. Through the finite element model method, the cable monitoring model based on distributed fiber optic sensing is constructed.

(2) With the technical support of the model proposed in this paper, design the electric-coupled finite element simulation experiments as well as temperature monitoring. It is found that more obvious buffer layer ablation fault characteristics can be observed by monitoring the temperature characteristics, which provides a reference for the wide application of this characteristic in practical monitoring.

(3) In the temperature monitoring of the cable state, the monitoring system equipped with the model of this paper can monitor the temperature change of the cable more accurately. In the K-fold cross-validation, the average accuracy of this paper's model in different datasets is as high as 92.4%, showing excellent generalization ability.

References

[1] Lin, B., & Zhu, J. (2020). Chinese electricity demand and electricity consumption efficiency: Do the structural changes matter?. Applied Energy, 262, 114505.

[2] Kumar, A. (2018). HVDC (high voltage direct current) transmission system: a review paper. Gyancity Journal of Engineering and Technology, 4(2), 1-10.

[3] Hafeez, K., & Khan, S. A. (2019). High voltage direct current (HVDC) transmission: Future expectation for Pakistan. CSEE Journal of Power and Energy Systems, 5(1), 82-86.

[4] Deng, D., Yuan, H., Cui, Y., & Ju, Y. (2018). Energy management of WSN-based charge measurement system of ultra high-voltage direct-current transmission line. Wireless Networks, 24, 1667-1681.
[5] Tarakesh, K. M. M., Chudamani, C., Dinesh, D., & Priyanka, B. (2022). Review On High Voltage Direct Current (Hvdc) Transmission System. Journal of Pharmaceutical Negative Results, 13.
[6] Vural, A. M. (2016). Contribution of high voltage direct current transmission systems to inter-area oscillation damping: A review. Renewable and Sustainable Energy Reviews, 57, 892-915.
[7] Koondhar, M. A., Kaloi, G. S., Saand, A. S., Chandio, S., Ko, W., Park, S., ... & El-Sehiemy, R. A. (2023). Critical technical issues with a voltage-source-converter-based high voltage direct current transmission system for the onshore integration of offshore wind farms. Sustainability, 15(18), 13526.
[8] Cui, Y., Song, X., Zhao, L., Yuan, H., Wu, G., & Wang, C. (2019). WSN-based measurement of ion-current density under high-voltage direct current transmission lines. IEEE Access, 7, 10947-10955.
[9] Swetapadma, A., Chakrabarti, S., Abdelaziz, A. Y., & Alhelou, H. H. (2021). A novel relaying scheme using long short term memory for bipolar high voltage direct current transmission lines. IEEE Access, 9, 119894-119906.
[10] Li, Z., & Du, B. (2018). Polymeric insulation for high-voltage dc extruded cables: challenges and development directions. IEEE Electrical Insulation Magazine, 34(6), 30-43.
[11] Mauseth, F., & Haugdal, H. (2017). Electric field simulations of high voltage DC extruded cable systems. IEEE Electrical Insulation Magazine, 33(4), 16-21.
[12] Mazzanti, G. (2017). Life and reliability models for high voltage DC extruded cables. IEEE Electrical Insulation Magazine, 33(4), 42-52.
[13] Andritsch, T., Vaughan, A., & Stevens, G. C. (2017). Novel insulation materials for high voltage cable systems. IEEE Electrical Insulation Magazine, 33(4), 27-33.
[14] Andersson, M. G., Hynynen, J., Andersson, M. R., Englund, V., Hagstrand, P. O., Gkourmpis, T., & Mu¨ller, C. (2017). Highly insulating polyethylene blends for high-voltage direct-current power cables. ACS Macro Letters, 6(2), 78-82.
[15] Smeets, R. P., & Belda, N. A. (2021). High‐voltage direct current fault current interruption: A technology review. High Voltage, 6(2), 171-192.
[16] Leterme, W., & Van Hertem, D. (2018). Cable protection in HVDC grids employing distributed sensors and proactive HVDC breakers. IEEE Transactions on Power Delivery, 33(4), 1981-1990.
[17] Kwon, G. Y., Lee, C. K., Lee, G. S., Lee, Y. H., Chang, S. J., Jung, C. K., ... & Shin, Y. J. (2017). Offline fault localization technique on HVDC submarine cable via time–frequency domain reflectometry. IEEE Transactions on Power Delivery, 32(3), 1626-1635.
[18] Dong, X., Yang, Y., Zhou, C., & Hepburn, D. M. (2017). Online monitoring and diagnosis of HV cable faults by sheath system currents. IEEE Transactions on Power Delivery, 32(5), 2281-2290.
[19] Li, R., & Xu, L. (2018). Review of DC fault protection for HVDC grids. Wiley Interdisciplinary Reviews: Energy and Environment, 7(2), e278.
[20] Khaimar, A. K., & Shah, P. J. (2016, December). Study of various types of faults in HVDC transmission system. In 2016 International Conference on Global Trends in Signal Processing, Information Computing and Communication (ICGTSPICC) (pp. 480-484). IEEE.
[21] Zou, Y., Wang, X., Zhang, H., Liu, C., Zhou, Q., & Zhu, W. (2016, October). Traveling-wave based fault location with high grounding resistance for HVDC transmission lines. In 2016 IEEE PES Asia-Pacific Power and Energy Engineering Conference (APPEEC) (pp. 1651-1655). IEEE.
[22] Li, C., & He, P. (2018). Fault‐location method for HVDC transmission lines based on phase frequency characteristics. IET Generation, Transmission & Distribution, 12(4), 912-916.